D3.2 Holographic imaging and privacy driven acquisition methods

Quanfeng Wang, Alexander Paulus, Matthias Saurer, Thomas Eibert

Grant Agreement Number	101099491
Action Acronym	HOLDEN
Action Title	Ethical Design of Holography with Dense Wireless Networks (HOLDEN)
Funding Scheme	HORIZON-EIC-2022-PATHFINDEROPEN-01
Version date of the Annex I against which the assessment will be made	13/12/2022
Start date of the project	1/6/2023
Due date of the deliverable	31/07/2024
Actual date of submission	31/07/2024
Responsible	TUM
Contributors	TUM
Dissemination level	Public

European Innovation Council

Funded by the European Union

Funded by the European Union. Views and opinions expressed are, however, those of the author(s) only and do not necessarily reflect those of the European Union or European Innovation Council and SMEs Executive Agency (EISMEA). Neither the European Union nor the granting authority can be held responsible for them. Grant Agreement No: 101099491.

Authors in alphabetical order

Full Name	Organisation	E-mail
Quanfeng Wang	TUM	quanfeng.wang@tum.de
Alexander Paulus	TUM	a.paulus@tum.de
Matthias Saurer	TUM	matthias.saurer@tum.de
Thomas Eibert	TUM	eibert@tum.de

Change History

Version	Date	Status	Author (Company)	Description
1.0	21.07.2024	Final	TUM	First final version

Executive Summary

Microwave imaging technologies, due to its non-ionizing nature and ability to penetrate dielectric materials, have been extensively studied over the past few decades. Corresponding applications are found in many fields, such as concealed weapons detection, non-destructive testing, and earth remote sensing. Moreover, microwave imaging shows advantages over optical cameras in terms of privacy protection due to an inherently lower spatial resolution, which alleviates compliance with privacy issues and ethical requirements. Meanwhile, the concept of passive radar imaging is gradually gaining attention in the imaging field as well. Compared to active radar imaging, passive radar uses ubiquitous electromagnetic waves as imaging sources, such as Wi-Fi signals, without the need for a dedicated transmitter. This characteristic has many advantages, since additional economic cost and extra pollution to the already increasingly crowded frequency bands is avoided. However, at the same time, a practical utilization of the passive imaging concept is challenging due to possibly non-coherent measurement signals, complex environments in which the wave propagation takes part, and the requirement of robust yet efficient imaging algorithms. Besides the technical aspects, also privacy and relevant ethical issues should be addressed properly in order to predict and avoid potential abuse of the proposed technology. We have considered privacy and ethical design in two main aspects, data collection and imaging algorithms. Although this is only a preliminary exploratory attempt, the technology still has significant room for optimization and improvement. Therefore, privacy considerations should be concurrently addressed in future developments.

Based on the concerns (and potential opportunities) that have been collected and expressed by all project partners in the ethics status monitor (ESM), we propose in this deliverable a privacy-compliant 3D holographic imaging algorithm based on the concept of passive radar. The algorithm utilizes a single-frequency inverse source reconstruction technique and achieves multiple-frequency imaging through the appropriate combination of single-frequency images via a sophisticated phase correction approach. In passive imaging, the electromagnetic field emitted by the source, which, for instance, can simply be a Wi-Fi access point after being scattered by the target of interest (TOI) or parasitic scatterers in the environment, e.g., wall or ground reflections, is collected by one or more receiving antennas. Employing our powerful inverse source solver, the fast irregular antenna field transformation algorithm (FIAFTA), the equivalent sources representing the transmitting antenna, the TOI, and parasitic scatterers are reconstructed, allowing for the separation and individual imaging of these objects. As such, the careful selection of potential source regions in the 3D imaging space already facilitates spatial filtering of the scene to be imaged and, thus, serves as an important tool for ensuring privacy compliance within our algorithm.

To fully enhance the benefits derived from wider frequency bands for improving imaging quality, the aforementioned phase correction methodology is utilized. This method is designed to facilitate the coherent summation of single-frequency images into a multiple-frequency image. The phase correction is based on wave propagation properties, compensating for phase shifts between sources and scatterers, as well as for delays caused by long cables in practical measurements. This phase correction method allows a focusing or defocusing of certain areas of the reconstructed image in a post-processing step and can be considered as a second intervention for preserving

possible privacy constraints and ethical guidelines. During the data collection process and again also during the imaging process, beamforming methodologies are another way of implementing privacy constraints and the final images can of course be filtered with respect to the privacy implications.

The following contents are covered:

- Short introduction of the HOLDEN project and the collaboration partners
- Reviewing of the microwave imaging technique and the concept of passive radar
- Theory of single-frequency inverse source reconstruction and image generation
- Phase correction method for multi-frequency imaging
- Numerical simulations and experimental measurements results
- Acquisition approaches by mechanical scanners and by drones
- Privacy and ethical considerations

Table of Contents

Abbreviations

Abbreviation	Description
3D	three-dimensional
Aalto	Aalto University
BPA	back projection algorithm
CNR	Consiglio Nazionale Ricerche
DVB	digital television broadcasting
EC	European Commission
EM	electromagnetic
ESM	Ethics Status Monitor
EU	European Union
FEM	finite element method
FFT	fast Fourier transform
FIAFTA	fast irregular antenna field transformation algorithm
GNSS	global navigation satellite systems
HE	Horizon Europe
HOLDEN	ethical design of holography in dense wireless networks
MIMO	multiple input multiple output
MLFMM	multilevel fast multipole method
MoM	method of moments
PEC	perfect electrically conductor
PWS	plane-wave spectrum
RF	radio frequency

SAR	synthetic aperture radar
SNR	signal-to-noise ratio
TOI	target of interest
TUM	Technical University of Munich
TWE	University of Twente
WP	work package

1. Introduction

1.1. About HOLDEN

The ubiquitous perception by sensing of objects, subjects and gestures is a pivotal challenge for future technology: it enables personalized services such as smart living, automated logistics or interaction through free-space gestures. However, it also challenges ethical and moral boundaries and threatens privacy. HOLDEN proposes a radically new approach to perception by concisely analysing ethical constraints and privacy risks while re-thinking RF-based sensing. We establish necessary conditions for privacy preserving and ethically compliant sensing and develop new paradigms respecting these constraints.

For the first time ever, HOLDEN constitutes a concentrated effort to explore social aspects of RF-sensing to guide the technological advance and to derive technology for ethically and privacy compliant perception. Central to HOLDEN is the development of ethical and privacy constraints. We use these findings to derive privacy and ethically compliant concepts for RF-based perception. We will develop a system of distributed multi-antenna devices for simultaneous multitarget recognition and ubiquitous perception with unprecedented accuracy, which constitutes a radical paradigm shift from a technology-centric perspective to a privacy-centric one via privacy by design.

HOLDEN achieves this goal along three high risk, complementary, and privacy-centric paths:

Path 1: Continuous-space measurement points: Radio-based 3D vision by holographic image processing of RF wavefronts.

Path 2: Discrete-space measurement points: Advanced 3D beamforming for human-scale recognition and tracking through dense massive connected antenna arrays.

Path 3: Signal processing and learning: High-dimensional tensor processing for the distinction of complex activities and motion from massive-dimensional RF data. The resulting breakthrough approaches and algorithms will be compared against application-level benchmarks via usage scenarios in the fields of logistics, smart living, and free-space

1.2. Partners

The consortium consists of four academic partners and a high-tech SME partner: (a) Aalto University (AALTO), Finland, (b) Technical University of Munich (TUM), Germany, (c) Consiglio Nazionale Ricerche (CNR), Italy, (d) University of Twente (TWE), Netherlands, and (e) Adant (Adant), Italy. This consortium features the specialized and complementary expertise required to achieve the project objectives. AALTO will be responsible for the project management (WP1), covered by an experienced and dedicated project manager. Ethical aspects (WP2), will be addressed by TWE (Prof. Ciano Aydin) who is a pioneer in the field. In particular, eventual gender differences in the ethical perception will be taken into account. TUM pioneered RF holography, which makes TUM (Prof. Thomas Eibert) the ideal leader of WP3. In advanced distributed signal and information processing, CNR has through Prof. Stefano Savazzi and Vittorio Rampa more than 14 years of

experience. CNR will lead WP4. Since more than 10 years, AALTO is active in radio sensing and machine learning based activity recognition. This expertise makes AALTO (Prof. Sigg) the ideal leader of WP5. Adant (Daniele Piazza) will contribute to the market analysis, application possibilities, and validation (WP6). Led by AALTO, dissemination with the website as one the media will be addressed by all partners. All academic partners are committed to early publication of results, e.g., via arXiv (open science).

2. Fundamentals of Microwave Imaging

Over the past decades, microwave imaging techniques have gathered considerable interest due to their many advantageous properties. Microwave radiation is non-ionizing and capable of penetrating through dielectric materials and walls, which make it suitable for a variety of imaging applications including but not limited to medical diagnostics [1]–[3], remote sensing [4], [5], security inspections [6], [7], homeland security [8], as well as earth remote sensing [9].

Microwave imaging technologies utilize discrete samples of the electromagnetic fields in spatially confined measurement areas and aim to reconstruct the shape, size, material properties, and location of unknown scattering objects in a given environment. This process, which can be for example realized by means of an inverse source reconstruction, therefore, seeks a solution to Maxwell's equation based on the measurements that were taken. Furthermore, an important concept in this regard is the Huygens' principle, which states that every radiation source can be represented in terms of equivalent sources, which produce the same observation samples. Hence, the goal of inverse source reconstructions is always to find the equivalent sources of a radiator or a scattering object. In a numerical implementation, different options are available, for instance, a plane-wave representation, a representation with respect to spherical multipoles, or a discretization in terms of equivalent currents of the unknown source distributions, which offers great flexibility in the solution process. After discretization of the unknown sources in terms of a superposition of basis functions, e.g., a plane-wave expansion and discretization of the forward operator, which establishes a relationship between the equivalent sources and the measurement samples, a linear system of equations is obtained.

In our work, iterative solvers such as the generalized minimal residual algorithm (GMRES) are employed to solve the linear system of equations, which has the advantage that an explicit formation of the forward operator in terms of a matrix representation is avoided and instead only repeated evaluations of matrix-vector products are required. In contrast to RF sensing [11] [12], where the goal is simply to detect whether an object or a person is present, we focus our research on microwave imaging, meaning creating snapshot images of an environment, which allows us to visually "see" the TOI.

2.1. Imaging Mechanisms and Algorithms

One of the most well-known imaging techniques is the synthetic aperture radar (SAR) approach [13], [14], which is based on digitally processing radar signals obtained at different measurement positions to form a larger synthetic aperture for higher resolution. One of the most common imaging mechanisms in SAR imaging is a monostatic setup, where the transmitter and receiver are collocated or placed very close to each other. Therefore, to collect measurements, one simple approach following the SAR principle is to use a single transceiver to scan the entire domain of interest, e.g., in a planer arrangement [15], which can, of course, be a time-consuming process. In contrast, a 2D array consisting of densely arranged antennas can be used as an alternative [16], but this array can be much more expensive due to the fact that more dedicated hardware is required.

Another widely used imaging approach is a multiple-input-multiple-output (MIMO) setup, where individual transmitters and receivers are distributed in the observation domain without the need to physically move any of the antennas [17]. The MIMO imaging mechanism can reduce the number of required scanning antennas to some degree while achieving the same lateral image resolution, but it also necessitates more sophisticated imaging algorithms. There are many interesting research efforts aiming to improve scanning mechanisms with fewer measurement antennas and, thus, sparser sampling [19], however, these are not in the scope of this deliverable. In this deliverable, the major focus is on the reconstruction process of the microwave images by utilizing an inverse source algorithm. In traditional SAR imaging, one of the most well-known methods is the back-projection algorithm (BPA), also referred to as the delay-and-sum method [20], meaning the image is created by coherently summing up the phase conjugated scattering data. While the BPA method can be easily implemented and is usually very robust, it requires a lot of computational resources. Contrary to our method, the BPA is an adjoint imaging method, meaning the spatial image is created in a few simple steps similar to the functionality of a matched filter. Further, the back-projection of the scattering data from the synthetic aperture towards the imaging domain can also be performed in the spatial frequency domain as utilized in the corresponding $\omega - k$ algorithms [21]. While the $\omega - k$ algorithms are mathematically equivalent to the BPA, they can be implemented with much more efficiency due to the utilization of fast Fourier transforms (FFTs) in the case of regularly sampled grids or by employing non-uniform FFTs in the case of irregularly distributed samples on a 2D grid [22]. Important to note is that the matched filter-based approaches identify potential peaks from the received signals via correlation operations [23]. Although widely utilized in imaging, they may not necessarily represent the actual physical process [24]. Alternatively, inverse equivalent sources reconstruction methods have shown numerous advantages, such as their flexibility in choosing the basis functions, the capability to handle irregular measurement grids as well as spatially undersampled data, the ability for full probe correction, and optimal numerical cost by utilizing diagonal operators and hierarchical structures such as employed in the multi-level fast multipole method (MLFMM) [25]-[29]. Therefore, in this deliverable, the inverse source reconstruction method is the preferred tool for image reconstruction and will be introduced in more detail in Section 3. By just performing one single iteration of the inverse source solver, an adjoint imaging approach can also be realized and utilized within a hybrid imaging methodology. As such, the imaging domain is scanned first by adjoint imaging and subsequently high-quality images of the TOIs are generated with the inverse source approach.

2.2. Passive Radar Imaging

In HOLDEN, the fundamental idea is to utilize the already existing Wi-Fi or cellular networks and extend their capabilities beyond communication to sensing and possibly imaging. Therefore, traditional active imaging principles cannot be applied easily since there is simply no 'active' source that would allow the establishment of a coherent phase relationship. Instead, as pointed out in the ESM, we just want to 'listen' to the already existing communication in the network as any other Wi-Fi device in the system by using measurements of a single (moving) or of many receiving antennas, which is very similar to the concept of passive imaging.

Passive radar has steadily gained popularity since its initial conception in 1935 [30], [31]. Compared to active radar, the most significant advantage of passive radar is, as already mentioned, its capability for detection and imaging without requiring a dedicated transmitter. This approach also avoids contributing additional pollution to the increasingly congested electromagnetic spectrum. Recent research has expanded passive radar target detection and imaging techniques to explore signals from various infrastructures, including global navigation satellite systems (GNSS) [32]–[34], digital television broadcasting (DVB)-T transmitters [35]–[38], DVB-S transmitters [39], [40], 5G network base stations [41]–[43] and Wi-Fi networks [44]–[47].

The use of non-cooperative radar signals presents challenges in achieving acceptable signal-to-noise ratios (SNRs) and in extracting target echoes from strong clutter echoes [48]. In a typical passive radar system, the processing of received signals generally involves two critical steps [30]. The first is direct signal interference and clutter cancellation [44], [48], [50], [51]. This step typically requires a fixed antenna to receive the reference signal and subsequently subtract the direct signal from the received surveillance signals. The second step involves extracting the potential echo of the TOI from the interference-cancelled signal often achieved through methods such as matched filters [48], [52].

In our approach, the utilized inverse source reconstruction techniques achieve these two processes simultaneously. This approach uses measurements of the radiated fields to reconstruct the equivalent sources of both the illuminating antenna and the scatterer. Throughout this process, all the benefits of the inverse equivalent source reconstruction methods as previously mentioned are preserved through the use of our potent inverse source solver, namely the fast irregular antenna field transformation algorithm (FIAFTA) [25]–[29]. To leverage the benefits of wider bandwidth in imaging, e.g., larger SNR and better range resolution, we utilize a corresponding phase correction method to combine the images obtained at different frequencies. Due to the propagation of electromagnetic waves from their sources towards the surface of a scattering object, which results in phase differences, a simple superposition of these single-frequency images can lead to a significant deterioration in the image quality if this phase delay is not considered appropriately.

Our phase correction method, on the other hand, facilitates coherent superposition of data from multiple frequencies in a simple post-processing step, thereby enabling superior imaging results. In addition to numerical simulations, the phase correction method has been further developed to compensate for delays encountered in practical measurements, particularly those caused by long cable lengths and measurement instrumentation. As mentioned earlier, this phase correction can also be used as a privacy-compliant filter operation by focusing and defocusing specific areas in the reconstructed image.

3. Passive Holographic Imaging

3.1. Single-Frequency Inverse Source Reconstruction

Consider the imaging configuration as illustrated in Fig. 1. An incident electric field $\vec{E}_{\mathrm{i}}$, which is created by the illuminating antenna, and the electric field $\vec{E}_{\mathrm{s}}$, which is scattered by the TOI, are represented by unknown spatial equivalent source distributions $\vec{J}_{\mathrm{i}}(\vec{r}')$ in V_{i} and $\vec{J}_{\mathrm{s}}(\vec{r}')$ in V_{s} , respectively.

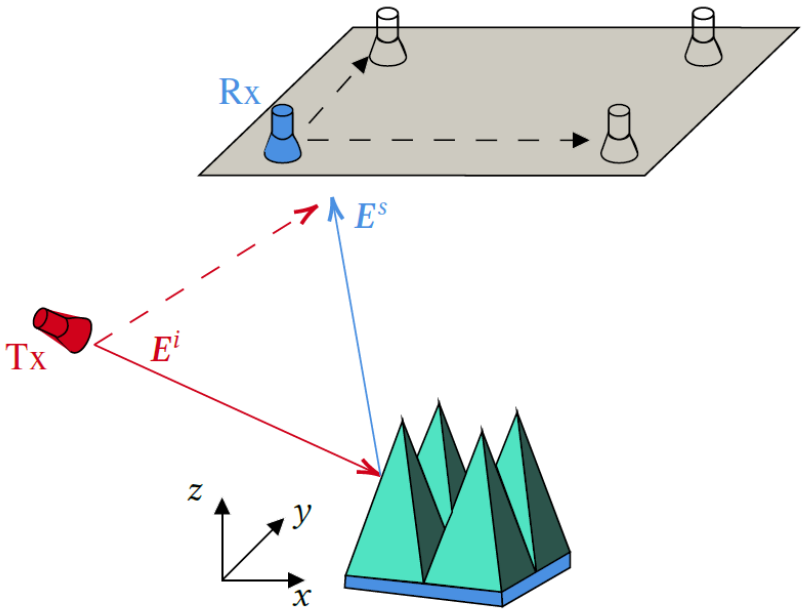

Fig. 1. Imaging configuration of the TOI using a single illumination source Tx. The fields received by the probe Rx is a superposition of $\vec{E}_i$ and $\vec{E}_S$. ©2024, IEEE

Denoting the observation and source locations by $\vec{r}$ and $\vec{r}'$, respectively, the observation signals at the probe output can be expressed as (assuming a time dependency of $\mathrm{e}^{\mathrm{j}\omega t}$) [29]

$$U(\vec{r}_m) = \iiint_{V_w} \vec{w}(\vec{r}-\vec{r}_m)\cdot\Big[\iint_{V_i} \vec{\vec{G}}(\vec{r},\vec{r}')\cdot\vec{J}_i(\vec{r}')\,\mathrm{d}a' + \iint_{V_s} \vec{\vec{G}}(\vec{r},\vec{r}')\cdot\vec{J}_s(\vec{r}')\,\mathrm{d}a'\Big]\mathrm{d}v, \tag{3.1}$$

where $\vec{w}(\vec{r}-\vec{r}_m)$ is a weighting function defined within the probe volume V_w representing the probe receiving behavior. $\vec{\vec{G}}(\vec{r},\vec{r}')$ denotes the dyadic free-space Green's function, which reads as

$$\vec{\vec{G}}(\vec{r},\vec{r}') = -\mathrm{j}\frac{\omega\mu}{4\pi}\left(\vec{\vec{\mathrm{I}}}+\frac{1}{k^2}\nabla\nabla\right)\frac{\mathrm{e}^{-\mathrm{j}k|\vec{r}-\vec{r}'|}}{|\vec{r}-\vec{r}'|}, \tag{3.2}$$

where k is the wavenumber in free space, μ denotes the permeability of free space and $\ddot{\mathrm{I}}$ is the unit dyad. By employing the fast multipole translation operator in conjunction with source cluster locations $\vec{r}_{\mathrm{s}}'$ or $\vec{r}_{\mathrm{i}}'$ to expand the scalar Green's function, an alternative representation based on propagating plane waves is given as

$$U(\vec{r}_m) = \frac{-\mathrm{j}}{4\pi} \iint \tilde{w}\left(-\vec{k}\right) \cdot T_L\left(\vec{k}, \vec{r}_m - \vec{r}_{\mathrm{i}}'\right) \tilde{J}_{\mathrm{i}}(\vec{k}) \, \mathrm{d}^2\hat{k} + \frac{-\mathrm{j}}{4\pi} \iint \tilde{w}\left(-\vec{k}\right) \cdot T_L\left(\vec{k}, \vec{r}_m - \vec{r}_{\mathrm{s}}'\right) \tilde{J}_{\mathrm{s}}(\vec{k}) \, \mathrm{d}^2\hat{k}. \tag{3.3}$$

The vector $\vec{k} = k\hat{k}$ is the wave vector decomposed into wavenumber k and unit vector $\hat{k}$. The order L of the translation operator T depends on the spatial extent of the corresponding source boxes and must be carefully chosen to achieve a desired level of accuracy, which, however, is controllable. In this equation, both the probe weighting $\vec{w}$ and the equivalent current density $\vec{J}$ are transformed into propagating plane-wave expansions according to [29]

$$\tilde{w}(\vec{k}) = \iiint_{V_w} \vec{w}(\vec{r} - \vec{r}_m) \mathrm{e}^{\mathrm{j}\vec{k}\cdot(\vec{r} - \vec{r}_m)} \, \mathrm{d}v \tag{3.4}$$

and

$$\tilde{J}_{\mathrm{i/s}}(\vec{k}) = -\mathrm{j}\frac{\omega\mu}{4\pi} \iiint_{V_{\mathrm{i/s}}} \left(\ddot{I} - \hat{k}\hat{k}\right) \cdot \vec{J}_{\mathrm{i/s}}(\vec{r}') \mathrm{e}^{\mathrm{j}\vec{k}\cdot(\vec{r}' - \vec{r}_{\mathrm{i/s}}')} \, \mathrm{d}v'. \tag{3.5}$$

In order to reduce the degrees of freedom and to enhance the conditioning of the resulting systems of equations, which both lead to faster convergence of the inverse source solver, the directive vector spherical harmonics $\vec{D}_{nm}^{(1/2)}$, introduced in [53], are employed throughout this paper to expand the equivalent sources at different frequencies.

However, for the sake of brevity and without any loss of generality, the ensuing discussion will primarily focus on the transverse electric (TE) and transverse magnetic (TM) vector spherical harmonics. Therefore, $\tilde{J}$ can be expanded in the form of [29]

$$\tilde{J}(\hat{k}) = \sum_{n=1}^{N} \sum_{m=-n}^{n} \left[c_{nm}^{\mathrm{TM}} \vec{n}_{mn}(\hat{k}) + c_{nm}^{\mathrm{TE}} \vec{m}_{mn}(\hat{k}) \right], \tag{3.6}$$

where c_{nm}^{TM} and c_{nm}^{TE} represent unknown expansion coefficients that can be determined by taking measurements, which consequently leads to a linear system of equations. The vector spherical harmonics $\vec{m}_{mn}$ and $\vec{n}_{mn}$ of degree n and order m are defined as [54], [55]

$$\vec{n}_{mn}(\hat{k}) = \frac{1}{\sqrt{n(n+1)}} \left(\frac{\partial \mathrm{Y}_{nm}(\hat{k})}{\partial \vartheta} \hat{e}_{\vartheta} + \frac{1}{\sin\vartheta} \frac{\partial \mathrm{Y}_{nm}(\hat{k})}{\partial \varphi} \hat{e}_{\varphi} \right), \tag{3.7}$$

$$\vec{m}_{mn}(\hat{k}) = \frac{1}{\sqrt{n(n+1)}} \left(\frac{\partial \mathrm{Y}_{nm}(\hat{k})}{\partial \vartheta} \hat{e}_{\varphi} - \frac{1}{\sin\vartheta} \frac{\partial \mathrm{Y}_{nm}(\hat{k})}{\partial \varphi} \hat{e}_{\vartheta} \right), \tag{3.8}$$

where $\hat{e}_{\vartheta}$ and $\hat{e}_{\varphi}$ are the spherical unit vector in ϑ- and φ- direction, respectively, and $\mathrm{Y}_{nm}(\hat{k})$ are the normalized spherical harmonics defined as

$$\mathrm{Y}_{nm}(\hat{k}) = \sqrt{\frac{(2n+1)(n-m)!}{4\pi(n+m)!}}\mathrm{P}_n^m(\cos\vartheta)\mathrm{e}^{\mathrm{j}m\varphi} \tag{3.9}$$

with the associated Legendre polynomials P_n^m. Combining the above equations allows to write (3.3) in a discretized form as the linear system of equations

$$Ax = b, \tag{3.10}$$

where the unknown expansion coefficients and the near-field measurement data U are stored in x and b, respectively. The matrix A is a linear operator that establishes the connections between the sources and the observations and is the numerical equivalent of the forward operator of the inverse source problem.

The linear equation (3.10) is solved in the form of a normal-error normal equation by the GMRES solver [56], [57]. This equivalent source reconstruction process, which is incorporated into FIAFTA [25]-[29], achieves high computational efficiency through the utilization of the MLFMM principle, which is based on a hierarchical and diagonal representation of the forward operator. Additionally, it enables us to distinguish easily between the radiating contributions from the source antenna, TOI, and other potential scatterers. In this approach, the scattered field from the TOI is selectively extracted while simultaneously suppressing direct interference from the illuminating source and any other potential clutter that may be present. This procedure involves the two essential steps previously mentioned and commonly found in most passive radar imaging techniques [44], [48], [50], [51], meaning cancellation of direct signal interference including also clutter and the extraction of the target signal.

Overall, the imaging algorithm based on inverse equivalent source reconstruction is executed in two stages. In the first stage, the plane-wave spectrum (PWS) of the TOI, the illuminating source, and any other potential echo scatterers are recovered and de-coupled based on the near-field measurements. This step is carried out at each single frequency. In the second stage, the PWS extracted from the TOI, which is nothing else than its equivalent representation in the spatial frequency domain, is utilized to generate the image of the TOI simply by combining all plane-wave contributions for every pixel in the discretized image domain. This is achieved by performing a hierarchical disaggregation scheme, which will be discussed in more detail in the following section. Overall, these two steps conclude the image generation for a single-frequency measurement. To create a multiple-frequency image, however, an appropriate phase correction is applied to each single-frequency image independently before they are summed up coherently.

3.2. Image Generation and Phase Correction

After solving the linear system of equations as stated in (3.10), the expansion coefficients for the directive vector spherical harmonics for the different source distributions are obtained, which then are utilized to compute $\tilde{J}_{\mathrm{i}}(\vec{k})$ as well as $\tilde{J}_{\mathrm{s}}(\vec{k})$ in accordance to (3.6). Therefore, discarding all constant factors that are not relevant for the image, the spatial equivalent current distributions can be evaluated based on

$$\vec{J}_{\mathrm{s},p}(\vec{r}') = \iiint_K \left(\vec{I} - \hat{k}\hat{k}\right) \cdot J_{\mathrm{s},p}(\vec{k})\, \mathrm{e}^{-\mathrm{j}\vec{k}\cdot(\vec{r}'-\vec{r}_s')}\,\mathrm{d}k, \tag{3.11}$$

where $p \in \{x, y, z\}$ indicates that the image generation is performed for the three different Cartesian vector components separately. In our work, a hierarchical disaggregation scheme is employed for the evaluation of (3.11) [58], which achieves the same optimal efficiency as FFT-based reconstruction but offers greater flexibility for the actual reconstruction points. Important to note is that the support region K in the spatial frequency is always restricted the available signal bandwidth and limited angular ranges. Consequently, as discussed in [59], the reconstructed sources are always a low-pass filtered version of the true source distribution, and this is the best we can hope for.

A minimum 4-term Blackman-Harris window function is chosen in this deliverable in order to suppress the ripples due to the hard band limitation at the Ewald boundary sphere, which lead to a lower amount of artifacts in the reconstructed image. As stated in (3.1) and (3.4), the probe receiver pattern is compensated by the weighting function $\vec{w}$. However, the characteristics of the illuminating source, e.g., its transmitting efficiency, which can vary with frequency and potentially lead to variations in the strength of the induced current densities at the surface of the scattering object, have not yet been considered. To address this discrepancy, the different single-frequency images are normalized by the total power within the observation area.

The phase correction terms for the source antenna and the scatterers require that their relative position with respect to each other is either known or can be estimated via the single-frequency images. Although the exact phase delay in the measurement cable is unknown, it is sufficient to ensure that the reconstructed phase of the source remains constant over frequency. A stronger illuminating source induces current densities with larger magnitudes on the scattering object, thus, possibly leading to improved imaging outcomes.

Assuming that the source is at position $\vec{r}_0'$ and that the phase change between the induced current and the exciting incident field is independent of frequency, the phase correction term for the TOI can be evaluated by compensating the line of sight propagation delay caused by the distance $|\vec{r}' - \vec{r}_0'|$ between the source and the TOI. Since this correction term is both frequency- and position-dependent, it can be applied to each pixel or voxel within the observation area to achieve coherent imaging for all potential equivalent source currents of the TOI.

3.3. Imaging Results

3.3.1. Numerical Results

For a first validation of the proposed inverse source technique, simulations were carried out using the commercial full-wave simulation software FEKO [60].

As illustrated in Fig. 2, a rectangular plate with some holes and rectangular cutouts is illuminated by a horn antenna under an angle of approximately 45 degrees. The plate is placed at the origin of the coordinate system, while the horn antenna is located at the coordinates x = 0.45 m, y = 0.45 m, z = 0 m. Both the antenna and the plate are made of perfectly electrically conducting (PEC) material. The length, width and thickness of the plate is 0.2 m, 0.2 m and 0.01 m, respectively. The x and z components of the electric field were collected over a rectangular aperture in the plane y = 1 m extending from x = −0.7 m, z = -0.5 m to x = 0.7 m, z = 0.5 m each sampled at 10 000 uniformly distributed points.

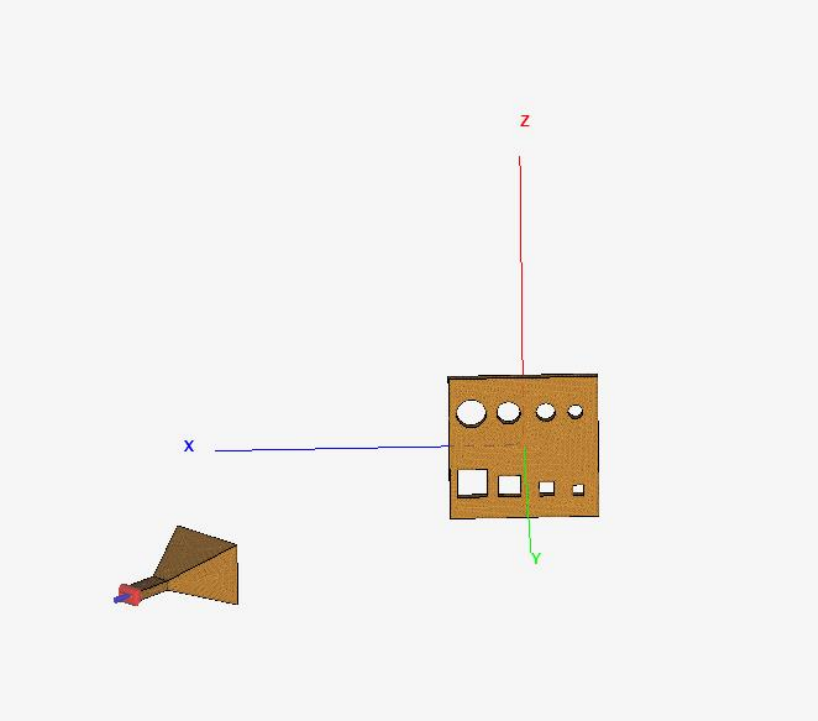

Fig. 2. Illustration of the simulation setup in FEKO including a rectangular plate as the scattering object and a horn antenna serving as the illumination source.

The utilized frequencies are linearly distributed from 8 GHz to 10 GHz with a step size of 50 MHz. The simulated electric field for the z-component is normalized to its maximum value and shown in Fig. 3(a), while the corresponding phase information is given in Fig. 3(b).

The image results for the horn antenna and the plate are shown in Fig. 4(a) and Fig. 4(b). Here, the spatial images are given in the planes y = 0.45 m for the horn antenna, and in the plane y = 0.01 m for the plate, which is identical to the location of the front side of the plate. These results show

a good focusing of both the horn antenna and the illuminated plate. Due to the chosen illumination configuration, the spatial image for the plate shows stronger scattering towards the positive x-axis, where, however, parts of the evaluation's patterns like the circular and rectangular cutouts are clearly visible. Compared to this, the reconstruction result employing the concept of back projection in the $\omega - k$ -domain as depicted in Fig. 4(c) shows less details and is mitigated by strong artifacts outside the region of the PEC plate. This nicely demonstrates the superiority of the employed inverse source based method over conventional adjoint imaging techniques.

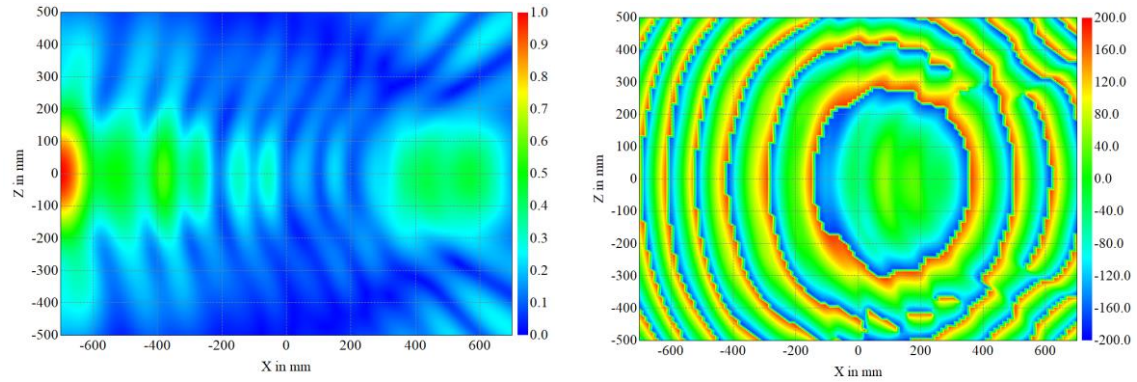

(a) (b)

Fig. 3. The simulated near-fields for the z-component of the electric field at 8 GHz. (a) The normalized magnitude. (b) The phase information.

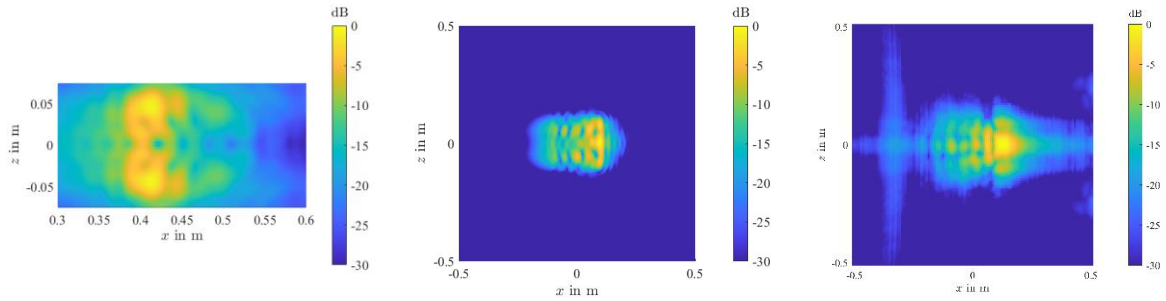

(a) (b) (c)

Fig. 4. Imaging results obtained by FIAFTA for the horn antenna and the metallic plate in (a) and (b), respectively. (c) Reconstruction result for the PEC plate employing back-projection in the $\omega - k$ -domain.

3.3.2. Measurement Results

To further demonstrate the excellent focusing properties of the proposed method, a measurement campaign was conducted in the anechoic antenna measurement chamber at the Chair of High-Frequency Engineering, Technical University of Munich. Two double-ridged horn antennas were utilized as the illuminating antenna and the scanning probe as depicted in Fig. 2. The probe was mounted on a planar scanner, which is capable of mechanically moving along the x- and y-

direction in the plane z = 2.8 m. Measurement samples of both co- and cross-polarized field components were taken at 11 110 different positions, uniformly distributed over a rectangular plane extending from x = −1.2 m, y = −1 m to x = 1.2 m, y = 1.2 m. The measurement frequency ranged from 6 GHz to 12 GHz with an equal frequency step of 50 MHz. Utilizing the FIAFTA allows for the simultaneous computation as well as separation of the PWS for both the horn antenna and the UAV, which served as the target in this scattering experiment. Additionally, the receiving behavior of the probe is comprehensively corrected using its known probe weighting coefficients.

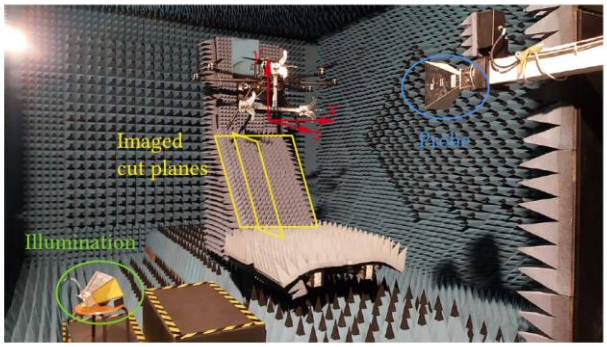

Fig. 5. Measurement configuration utilized in the anechoic chamber. The origin of the coordinate system is set close to the location where the UAV is placed. ©2024, IEEE

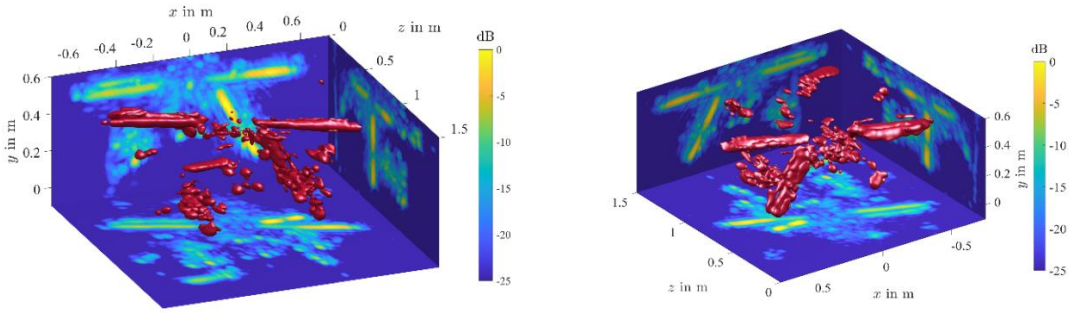

Fig. 6. 3-D visualization of the imaged UAV. (a) Viewed from a perspective oriented towards the negative z-direction. (b) Viewed from a perspective oriented towards the positive z-direction.

With appropriate phase correction facilitating coherent summation of the spatial imaging results across all frequencies, the final imaging results are presented in Fig. 6. The reconstruction area chosen for the UAV is constrained in a cubic space with the boundaries −0.75 m $\leqslant x \leqslant$ 0.75 m, −0.1 m $\leqslant y \leqslant$ 0.6 m and 0.0 m $\leqslant z \leqslant$ 1.5 m. For a more intuitive display, the scattering points with the same signal strength are created to show the outline of the UAV. In addition, the normalized current densities $\vec{J}_s(\vec{r}')$ are mapped onto the faces of the cuboid enclosing the imaging region via a maximum intensity projection. In these images, several key characteristics of

the illuminated UAV can be easily identified such as different parts of the metallic frame as well as parts of the rotor blades.

Additionally, we noticed that the absorbers in the anechoic chamber exhibit a weak scattering behavior, which, therefore, can be visualized by our powerful imaging method as well [61]. The normalized current density is displayed on two distinct cut planes, one parallel and the other perpendicular to the slope on which the absorbers are mounted, as illustrated in Fig. 7. Visually, separate pyramidal absorber elements can be identified. In Fig. 7(a) the absorbers on the left seem to be causing stronger reflections, however, this is due to their close proximity to the illuminating horn antenna relatively oblique electromagnetic field incidence angle.

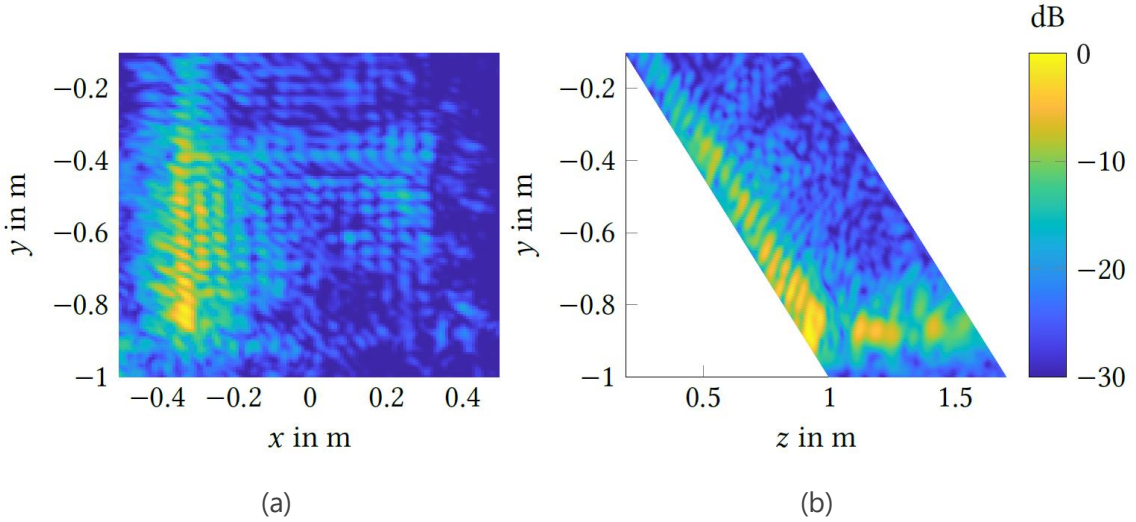

Fig. 7. Imaging results of the absorbers, (a) in plane parallel to the absorbers with $z = -0.9y + 0.2\,\mathrm{m}$, (b) in plane perpendicular to the absorbers with $x = -0.33$ m. ©2024, IEEE

3.4. Data Acquisition Approaches

Appropriate data acquisition approaches are crucial for the success of passive holographic imaging methodologies. On the long term, very high-speed acquisition approaches are needed, which are able to collect many measurement samples simultaneously, e.g., by massive antenna array technology. In the current research project, our goal is to demonstrate the technology by using prototypical data acquisition schemes, which typically collect the data over a large observation time by moving one or more measurement antennas through space. The first considered data acquisition prototype is our antenna measurement system as shown in Fig. 5. It has been adapted to the collection of passive imaging data and it allows to define the imaging environment in a very specific way, e.g., by placing microwave absorbers or by moving the TOI with the spherical scanner system. The second considered acquisition system is shown in Fig. 8. It is a planar scanner system installed in an office environment, which can be equipped with various antennas, and where the position of the moving antenna can be tracked with good accuracy. The scanner system is equipped with computer control and can automatically collect observation data as needed for our holographic imaging approach.

Fig. 8. Planar mechanical scanner system installed in an office environment with computer control and positioning approach.

The third considered type of imaging approach, which were set up for data acquisition are drone based measurement data collection systems as shown in Fig. 9. The drones are equipped with appropriate receiving antennas and positioning approaches based on satellite navigation or laser trackers are available.

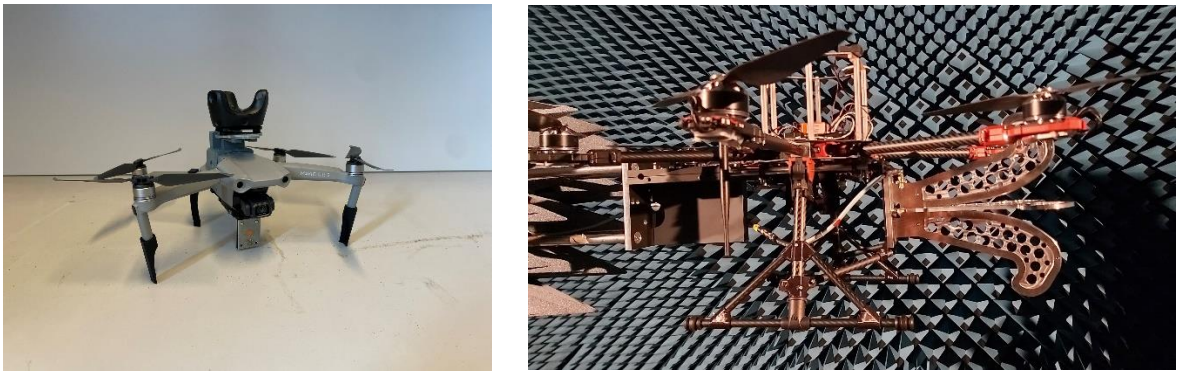

Fig. 9. Drone based data acquisition systems equipped with antennas, control, and positioning sensors.

3.5. Privacy and Ethical Considerations

Compared to optical imaging, microwave imaging technology offers more direct protection of user privacy and naturally alleviates ethical concerns. This advantage arises primarily because, as shown in Fig. 3, microwave imaging collects the amplitude and phase information of directly incident or scattered electromagnetic fields present in space. Without corresponding imaging or other sensing technologies, it is almost impossible to extract useful information about the real environment from this data. This imposes a significant technical barrier to obtain private information, which is a natural advantage of microwave imaging over optical imaging in terms of privacy protection.

Of course, with appropriate imaging technologies, it is possible to extract relevant environmental information from these data. However, due to the wavelength of the microwave band and the limited bandwidth in the passive radar imaging scenarios we consider, the resolution of the images is greatly restricted. The maximum resolution is limited at the physical level, which cannot easily be surpassed by imaging technology. Consequently, images obtained from microwave imaging lack all optical information such as color present in the real environment. Under such resolution limitations, identifying individuals becomes more difficult.

In our imaging algorithms, considerations of privacy and ethical issues can be further addressed in two key aspects. Firstly, regarding data collection, we can use highly directional antennas or beamforming technology to collect data only from user-specified areas, thereby avoiding the collection of sensitive data. Beamforming technology achieves high directivity in the reception antenna pattern by adjusting the phase, allowing it to receive electromagnetic fields only from specific directions. Information received through side lobes is difficult to use directly for imaging, ensuring that user privacy is protected to the extent specified by the user. Although this technical aspect is not demonstrated in the current deliverable, its implementation is straightforward in principle. In practical deployment and application, users should have significant flexibility to adjust the data collection area of the imaging system, allowing them to tailor the application of imaging technology according to their needs.

Secondly, and more importantly, our inverse source based imaging algorithm significantly empowers users with choice. As demonstrated in Fig. 6 and Fig. 7, in our measurement scenarios, although the scattered fields from the UAV and absorbers are measured during the data collection in the near-field measurements, we can specify the objects to be imaged during the inverse source reconstruction process. The scattered fields corresponding to other objects are completely filtered out and do not appear in the imaging results. In practical applications, users can configure the imaging algorithm to avoid imaging sensitive objects. This can also be achieved through passive identification methods. For example, by designing appropriate passive tags, when the imaging system detects the corresponding passive tag, the inverse source reconstruction algorithm can completely eliminate the electromagnetic field contribution of that part from the near-field measurement data, retaining only the desired information of the TOI. This functionality greatly enhances the flexibility of the imaging algorithm and improves privacy and ethical protection.

4. Summary

A comprehensive inverse equivalent source based method has been introduced to create spatial microwave images in a passive scattering environment. Utilizing the fast irregular antenna field transformation algorithm (FIAFTA) and employing the surface equivalence principle, which is also known as the Huygens' principle, an equivalent plane-wave representation of both the illuminating source and the target(s) of interest is computed. FIAFTA simultaneously accomplishes target signal extraction and echo suppression and is adaptable to arbitrary measurement configurations, including irregular sampling grids, while facilitating full probe correction. Moreover, the efficiency of the FIAFTA is significantly enhanced by utilizing a hierarchical computation scheme, which allows rapid evaluations of the radiation (scattering) operators. Assuming the validity of the first-order Born approximation, which allows a linearization of the otherwise non-linear scattering problem a linear system of equations is established, which is solved efficiently utilizing an iterative solver. After obtaining the plane-wave expansion coefficients for all pre-defined source boxes, their corresponding spatial images are obtained by a hierarchical disaggregation scheme. In the current implementation, the measurement data is processed separately for each frequency, hence, as an intermediate result, a spatial image is created for each frequency separately as well. In order to combine the different single-frequency images and obtain sharper images, a sophisticated phase correction method is employed, which compensates the phase delay between the transmitting antenna(s) and the scattering object(s) as well as phase delays introduced by the measurement equipment in real-world applications. Corresponding adjoint imaging approaches are immediately obtained from the inverse source solver by evaluating only one iteration, where hybrid imaging methodologies with adaptive speed and accuracy are also available.

Based on numerical experiments using simulation data obtained by the commercial software FEKO, we have not only shown the great focusing capabilities of the FIAFTA but also its superiority over adjoint imaging approaches, which especially struggle to de-couple the contributions from both the transmitting antenna(s) and the scattering objects for a given measurement set. Practical measurements conducted at our anechoic chamber demonstrate the real-world applicability of our method and the imaging of electrically large objects such as an uninhabited aerial vehicle. Interestingly, due to the high accuracy of our inverse source method, we are also able to distinguish strongly scattering objects from weakly scattering objects, which was illustrated by creating a spatial image of the absorbers inside the anechoic chamber. To mitigate privacy risks and to ensure the compliance with ethical guidelines two mechanisms for the inverse source based method were identified. Firstly, the FIAFTA requires the definition of possible source boxes inside the reconstruction volume, which inherently performs a spatial filtering. Therefore, only an image corresponding to these pre-defined source locations can be computed and scattering contributions stemming from outside these regions are filtered. Second, the phase correction method is based on a coherent superposition of the single-frequency images dependent on the specified pixel positions, which can, thus, be used for focus or defocusing different parts of the reconstructed images in a post-processing step. Utilizing both filter methods, the presented inverse source method not only yields a flexible yet efficient imaging algorithm but considers privacy and ethical related issues by design.

Data acquisition methods have been realized based on mechanical scanner systems and based on drones. High-quality measurement data can be collected in our anechoic chamber measurement environment. For the acquisition of realistic measurement data, a mechanical scanner system was set up in an office environment. Moreover, drone based measurement systems have been conceived and realized.

5. References

[1] S. S. Ahmed, A. Schiessl, F. Gumbmann, M. Tiebout, S. Methfessel, and L.-P. Schmidt, "Advanced microwave imaging," IEEE Microw. Mag., vol. 13, no. 6, pp. 26–43, Sep. 2012.

[2] R. Chandra, H. Zhou, I. Balasingham, and R. M. Narayanan, "On the opportunities and challenges in microwave medical sensing and imaging," IEEE Trans. Biomed. Eng., vol. 62, no. 7, pp. 1667–1682, Jul. 2015.

[3] H. Scudder, "Introduction to computer aided tomography," Proc. IEEE, vol. 66, no. 6, pp. 628–637, Jun. 1978

[4] K. E. Sawaya, L. G. Olmanson, N. J. Heinert, P. L. Brezonik, and M. E. Bauer, "Extending satellite remote sensing to local scales: Land and water resource monitoring using high-resolution imagery," Remote Sens. Environ., vol. 88, no. 1, pp. 144–156, Nov. 2003.

[5] D. Le Vine, "Synthetic aperture radiometer systems," IEEE Trans. Microw. Theory Tech., vol. 47, no. 12, pp. 2228–2236, Dec. 1999.

[6] S. S. Ahmed, "Microwave imaging in security — two decades of innovation," IEEE J. Microw., vol. 1, no. 1, pp. 191–201, Jan. 2021.

[7] D. Sheen, D. McMakin, and T. Hall, "Three-dimensional millimeter wave imaging for concealed weapon detection," IEEE Trans. Microw. Theory Tech., vol. 49, no. 9, pp. 1581–1592, Sep. 2001.

[8] J.-I. Park and K.-T. Kim, "A comparative study on ISAR imaging algorithms for radar target identification," Progress Electromagn. Res., vol. 108, pp. 155–175, 2010.

[9] R. S. Detrick, P. Buhl, E. Vera, J. Mutter, J. Orcutt, J. Madsen, and T. Brocher, "Multi-channel seismic imaging of a crustal magma chamber along the east pacific rise," Nature, vol. 326, pp. 35–41, Mar. 1987.

[10] X. Liu, J. Cao, S. Tang, J. Wen, and P. Guo, "Contactless respiration monitoring via off-the-shelf WiFi devices," IEEE Trans. Mobile Comput., vol. 15, no. 10, pp. 2466–2479, Oct. 2016.

[11] D. Salami, R. Hasibi, S. Palipana, P. Popovski, T. Michoel and S. Sigg, "Tesla-Rapture: A Lightweight Gesture Recognition System From mmWave Radar Sparse Point Clouds," IEEE Trans. Mobile Comput., vol. 22, no. 8, pp. 4946-4960, 1 Aug. 2023.

[12] H. Wang, D. Zhang, Y. Wang, J. Ma, Y. Wang, and S. Li, "RT-Fall: A real-time and contactless fall detection system with commodity WiFi devices," IEEE Trans. Mobile Comput., vol. 16, no. 2, pp. 511–526, Feb. 2017.

[13] A. Moreira, P. Prats-Iraola, M. Younis, G. Krieger, I. Hajnsek, and K. P. Papathanassiou, "A tutorial on synthetic aperture radar," IEEE Geosci. Remote Sens. Mag., vol. 1, no. 1, pp. 6–43, Mar. 2013.

[14] C. Ozdemir, Inverse Synthetic Aperture Radar Imaging With MATLAB Algorithms, 2nd ed. Hoboken, NJ, USA: Wiley-Interscience, Jun. 2021.

[15] S. Gu, C. Li, X. Gao, Z. Sun, and G. Fang, "Three-dimensional image reconstruction of targets under the illumination of terahertz Gaussian beam-theory and experiment," IEEE Trans. Geosci. Remote Sens., vol. 51, no. 4, pp. 2241–2249, Apr. 2013.

[16] Sheen, D. Mcmakin, and T. Hall, "Near-field three-dimensional radar imaging techniques and applications," Appl. Opt., vol. 49, no. 19, p. E83, 2010.

[17] S. S. Ahmed, A. Schiessl, and L.-P. Schmidt, "A novel fully electronic active real-time imager based on a planar multistatic sparse array," IEEE Trans. Microw. Theory Techn., vol. 59, no. 12, pp. 3567–3576, Dec. 2011.

[18] S. Wu et al., "MIMO-SA-Based 3-D Image Reconstruction of Targets Under Illumination of Terahertz Gaussian Beam—Theory and Experiment," IEEE Trans. Microw. Theory Tech., vol. 71, no. 9, pp. 4080-4097, Sept. 2023.

[19] A. V. Muppala and K. Sarabandi, "Low-Cost 3-D Millimeter-Wave Concealed Weapons Detection Using Single Transceiver Affine Synthetic Arrays," IEEE Trans. Microw. Theory Tech., vol. 71, no. 12, pp. 5445-5456, Dec. 2023

[20] H. L. Van Trees, Optimum array processing: Part 4 of detection, estimation, and modulation theory. Hoboken, NJ, USA: John Wiley & Sons, Inc., 2002

[21] C. Cafforio, C. Prati, and F. Rocca, "SAR data focusing using seismic migration techniques," IEEE Trans. Aerosp. Electron. Syst., vol. 27, no. 2, pp. 194–207, Mar. 1991.

[22] X. Zhuge and A. G. Yarovoy, "Three-dimensional near-field MIMO array imaging using range migration techniques," IEEE Trans. Image Process., vol. 21, no. 6, pp. 3026–3033, Jun. 2012.

[23] J. Gao, B. Deng, Y. Qin, H. Wang, and X. Li, "An efficient algorithm for MIMO cylindrical millimeter-wave holographic 3-D imaging," IEEE Trans. Microw. Theory Techn., vol. 66, no. 11, pp. 5065–5074, Nov. 2018.

[24] G. Turin, "An introduction to matched filters," IRE Trans. Inf. Theory, vol. 6, no. 3, pp. 311–329, Jun. 1960.

[25] W. M. G. Dyab, T. K. Sarkar, A. Garc´ıa-Lamp´erez, M. Salazar-Palma, and M. A. Lagunas, "A critical look at the principles of electromagnetic time reversal and its consequences," IEEE Antennas Propag. Mag., vol. 55, no. 5, pp. 28–62, Oct. 2013.

[26] C. H. Schmidt, M. M. Leibfritz, and T. F. Eibert, "Fully probe-corrected near-field far-field transformation employing plane wave expansion and diagonal translation operators," IEEE Trans. Antennas Propag., vol. 56, no. 3, pp. 737–746, Mar. 2008.

[27] C. H. Schmidt and T. F. Eibert, "Multilevel plane wave based near-field far-field transformation for electrically large antennas in free-space or above material half space," IEEE Trans. Antennas Propag., vol. 57, no. 5, pp. 1382–1390, May 2009.

[28] T. F. Eibert and C. H. Schmidt, "Multilevel fast multipole accelerated inverse equivalent current method employing Rao–Wilton–Glisson discretization of electric and magnetic surface currents," IEEE Trans. Antennas Propag., vol. 57, no. 4, pp. 1178–1185, Apr. 2009.

[29] T. F. Eibert, E. Kilic, C. Lopez, R. A. M. Mauermayer, O. Neitz, and G. Schnattinger, "Electromagnetic field transformations for measurements and simulations," PIER, vol. 151, pp. 127–150, 2015.

[30] H. Griffiths and N. Willis, "Klein heidelberg the — first modern bistatic radar system," IEEE Trans. Aerosp. Electron. Syst., vol. 46, no. 4, pp. 1571–1588, Oct. 2010.

[31] H. Kuschel, D. Cristallini, and K. E. Olsen, "Tutorial: Passive radar tutorial," IEEE Aerosp. Electron. Syst. Mag., vol. 34, no. 2, pp. 2–19, Feb. 2019.

[32] F. Santi, M. Bucciarelli, D. Pastina, M. Antoniou, and M. Cherniakov, "Spatial resolution improvement in GNSS-based SAR using multistatic acquisitions and feature extraction," IEEE Trans. Geosci. Remote Sens., vol. 54, no. 10, pp. 6217–6231, Oct. 2016.

[33] D. Pastina, F. Santi, F. Pieralice, M. Antoniou, and M. Cherniakov, "Passive radar imaging of ship targets with GNSS signals of opportunity," IEEE Trans. Geosci. Remote Sens., vol. 59, no. 3, pp. 2627–2642, Mar. 2021.

[34] C. Huang, Z. Li, H. An, Z. Sun, J. Wu, and J. Yang, "Passive multistatic radar imaging of vessel target using GNSS satellites of opportunity," IEEE Trans. Geosci. Remote Sens., vol. 60, pp. 1–16, 2022.

[35] Y. Fang, G. Atkinson, A. Sayin, J. Chen, P. Wang, M. Antoniou, and M. Cherniakov, "Improved passive SAR imaging with DVB-T transmissions," IEEE Trans. Geosci. Remote Sens., vol. 58, no. 7, pp. 5066–5076, Jul. 2020.

[36] D. Olivadese, E. Giusti, D. Petri, M. Martorella, A. Capria, and F. Berizzi, "Passive ISAR with DVB-T signals," IEEE Trans. Geosci. Remote Sens., vol. 51, no. 8, pp. 4508–4517, Aug. 2013.

[37] W. Qiu, E. Giusti, A. Bacci, M. Martorella, F. Berizzi, H. Zhao, and Q. Fu, "Compressive sensing–based algorithm for passive bistatic ISAR with DVB-T signals," IEEE Trans. Aerosp. Electron. Syst., vol. 51, no. 3, pp. 2166–2180, Jul. 2015.

[38] M. E. Nouar, O. Mahfoudia, A. Bouaraba, and X. Neyt, "Fast and efficient clutter cancellation approach for DVB-T based passive radars," PIER B, vol. 98, pp. 165–187, 2023.

[39] S. Brisken, M. Moscadelli, V. Seidel, and C. Schwark, "Passive radar imaging using DVB-S2," in 2017 IEEE Radar Conf. RadarConf, May 2017, pp. 0552–0556.

[40] S. Gutierrez-Serrano, M.-C. Benito-Ortiz, D. Mata-Moya, M.-P. Jarabo- Amores, and N. Del-Rey-Maestre, "Road traffic passive radar imaging using DVB-S," in 2022 23rd Int. Radar Symp. IRS, Sep. 2022, pp. 218– 223.

[41] J. Guan, A. Paidimarri, A. Valdes-Garcia, and B. Sadhu, "3-D imaging using millimeter-wave 5G signal reflections," IEEE Trans. Microw. Theory Tech., vol. 69, no. 6, pp. 2936–2948, Jun. 2021.

[42] P. Samczy´nski, K. Abratkiewicz, M. Płotka, T. P. Zieli´nski, J. Wszołek, S. Hausman, P. Korbel, and A. Ksie¸ ˙zyk, "5G network-based passive radar," IEEE Trans. Geosci. Remote Sens., vol. 60, pp. 1–9, 2022.

[43] S. Vakalis, S. Mghabghab, and J. A. Nanzer, "Fourier domain millimetre wave imaging using noncooperative 5G communications signals," IEEE Trans. Antennas Propag., vol. 70, no. 10, pp. 8872–8882, Oct. 2022.

[44] P. M. Holl and F. Reinhard, "Holography of Wi-Fi radiation," Phys. Rev. Lett., vol. 118, no. 18, p. 183901, May 2017.

[45] F. Colone, P. Falcone, C. Bongioanni, and P. Lombardo, "WiFi-based passive bistatic radar: Data processing schemes and experimental results," IEEE Trans. Aerosp. Electron. Syst., vol. 48, no. 2, pp. 1061– 1079, Apr. 2012.

[46] Y. He, Y. Chen, Y. Hu, and B. Zeng, "WiFi vision: Sensing, recognition, and detection with commodity MIMO-OFDM WiFi," IEEE Internet Things J., vol. 7, no. 9, pp. 8296–8317, Sep. 2020.

[47] W. Li, R. J. Piechocki, K. Woodbridge, C. Tang, and K. Chetty, "Passive WiFi radar for human sensing using a stand-alone access point," IEEE Trans. Geosci. Remote Sens., vol. 59, no. 3, pp. 1986–1998, Mar. 2021.

[48] F. Colone, D. W. O'Hagan, P. Lombardo, and C. J. Baker, "A multistage processing algorithm for disturbance removal and target detection in passive bistatic radar," IEEE Trans. Aerosp. Electron. Syst., vol. 45, no. 2, pp. 698–722, Apr. 2009.

[49] F. Colone, F. Filippini, and D. Pastina, "Passive radar: Past, present, and future challenges," IEEE Aerosp. Electron. Syst. Mag., vol. 38, no. 1, pp. 54–69, Jan. 2023.

[50] F. Colone, C. Palmarini, T. Martelli, and E. Tilli, "Sliding extensive cancellation algorithm for disturbance removal in passive radar," IEEE Trans. Aerosp. Electron. Syst., vol. 52, no. 3, pp. 1309–1326, Jun. 2016.

[51] P. Lombardo and F. Colone, "Advanced processing methods for passive bistatic radar systems," in Principles of Modern Radar: Advanced Techniques. IET Digital Library, Jan. 2012, pp. 739–821.

[52] P. Wojaczek, F. Colone, D. Cristallini, and P. Lombardo, "Reciprocal filter- based STAP for passive radar on moving platforms," IEEE Trans. Aerosp. Electron. Syst., vol. 55, no. 2, pp. 967–988, Apr. 2019.

[53] T. F. Eibert, M. M. Saurer, A. H. Paulus, and J. Knapp, "Inverse source solutions with simultaneous localization in the spatial and spectral domains–sparse sampling for directive antennas," IEEE Trans. Antennas Propag., pp. 1–1, 2023.

[54] J. E. Hansen, Spherical Near-Field Antenna Measurements (Electromagnetics and Radar Series), 2nd ed. London, U.K: Peregrinus, 1988.

[55] J. A. Stratton, Electromagnetic Theory. John Wiley & Sons, Jan. 2007.

[56] J. Kornprobst, R. A. Mauermayer, O. Neitz, J. Knapp, and T. F. Eibert, "On the solution of inverse equivalent surface-source problems," PIER, vol. 165, pp. 47–65, 2019.

[57] Y. Saad, Iterative Methods for Sparse Linear Systems, 2nd ed. Society for Industrial and Applied Mathematics, 2003.

[58] G. Schnattinger and T. F. Eibert, “Solution to the full vectorial 3-D inverse source problem by multilevel fast multipole method inspired hierarchical disaggregation,” IEEE Trans. Antennas Propag., vol. 60, no. 7, pp. 3325–3335, Jul. 2012.

[59] Devaney AJ. Mathematical Foundations of Imaging, Tomography and Wavefield Inversion. Cambridge University Press; 2012.

[60] Altair. (2023) FEKO. [Online]. Available: https://altairhyperworks.com/product/FEKO

[61] Q. Wang and T. F. Eibert, “Microwave imaging of electromagnetic wave absorbers in an antenna measurement chamber,” in IEEE Int. Symp. Antennas Propag., Florence, Italy, Jul. 2024, pp. 1–2.

6. Table of Figures